Journal of Thermal Analysis and Calorimetry (2025) 150:10935–10949
https://doi.org/10.1007/s10973-025-14430-2

Two novel energetic Ag(I) complexes: synthesis, crystal structure, and thermal investigations

Akın Er[1,2] · Çiğdem Ay[3] · Nurdane Yılmaz[4] · Sinecan İrem Bozkuş[5] · Nurcan Acar[6] · Başar Karaca[7] · Orhan Atakol[6]

Received: 5 November 2024 / Accepted: 18 May 2025 / Published online: 25 June 2025
© The Author(s) 2025

Abstract

Two crystalline silver(I) complexes were synthesized by combining the ligand tris(pyrazole-1-yl) methane (L_1) with silver chlorate, $[AgCH(C_3H_3N_2)_3.\ ClO_3]$ **(I)**, and 3,5-bis(pyridin-2-yl)-4-amino-1,2,4-triazole (L_2) with silver nitrate, $[AgC_2H_2N_4(C_5H_4N)_2]NO_3$ **(II)**. The complexes were characterized by elemental analysis, Fourier ransform infrared spectroscopy (FT-IR), and single-crystal X-ray diffraction analysis. The structures and unit cell parameters of the complexes were determined. In both complexes, the Ag(I) central atom was found to be coordinated in a highly distorted tetrahedral configuration. The nitrogen donors of neighboring ligands coordinated two different Ag(I) ions, resulting in a polynuclear structure. Thermogravimetric analysis (TGA) indicated that complex **I** underwent decomposition through a two-step thermal decomposition occurring between 160 and 250 °C, whereas complex **II** experienced a rapid exothermic reaction within a very limited temperature range. Thermokinetic parameters of decompositions were determined by non-isothermal/isoconvertional kinetic methods, Ozawa–Flynn–Wall (OFW), and Kissenger–Akahira–Sunose (KAS). Thermodynamic parameters were calculated from two steps of the thermal decomposition for complex **I** and one step for complex **II**.

Keywords Kissenger–Akahira–Sunose · Nitrogen-rich ligand · Ozawa–Flynn–Wall · Silver(I) complexes · Thermokinetic analysis

Introduction

Some Ag(I) salts, such as silver nitrotetrazolate [1], silver azide[2, 3], silver fulminate [4, 5], silver carbide [6, 7], silver oxalate [8], and complexes have long been known to be explosive at high temperatures [9, 10]. In Ag(I) complexes prepared with organic ligands, the complex inevitably behaves like an explosive substance if there are ions such as nitrate, chlorate, and perchlorate as free ions or auxiliary ligands [11–13]. Moreover, recent studies have highlighted the prominence of nitrogen-rich materials in the field of energetic substances [1, 14, 15]. These nitrogen-rich materials have shown promise in enhancing the explosive properties of Ag(I) complexes, making them potential candidates for advanced energetic applications. Enhancing the thermal, chemical, and frictional stability of energetic materials is a primary focus of current research efforts. Materials exhibiting energetic properties, characterized by a constrained thermal decay temperature range and increased thermal stability, are employed as initiators in ammunition applications. The study carried out by Atakol et al. demonstrated that

✉ Çiğdem Ay
cigdem.ay@dpu.edu.tr

1 Department of Chemistry, Graduate School of Natural and Applied Science, Ankara University, Ankara, Turkey

2 Department of Pharmacy Services, Gülhane Vocational School of Health, University of Health Sciences, Ankara, Turkey

3 Department of Chemistry, Faculty of Science and Arts, Kütahya Dumlupınar University, Kütahya, Turkey

4 Department of Mathematics and Science Education, Kastamonu University, Kastamonu, Turkey

5 Department of Forensic Sciences, Gendarmerie and Coast Guard Academy, Ankara, Turkey

6 Department of Chemistry, Faculty of Science, Ankara University, Ankara, Turkey

7 Department of Biology, Faculty of Science, Ankara University, Ankara, Turkey

nitrogen-rich complexes synthesized using $AgNO_3$ were predominantly single crystalline and displayed exothermic thermal decomposition within a limited temperature range. [12] (Fig. 1).

This research focuses on synthesizing novel nitrogen-rich Ag(I) complexes intended for use as initiators (detonators) that exhibit exothermic decomposition within narrow and high-temperature ranges. Accordingly, tris(pyrazole-1-yl) methane (L_1; $CH(C_3H_3N_2)_2$) and 3,5-bis(pyridin-2-yl)-4-amino-1,2,4-triazole (L_2; $C_2H_2N_4(C_5H_4N)_2$), which can be considered slightly rich in nitrogen, were chosen as ligands. L_1 performs as a widely utilized ligand in the formation of spin crossover complexes, and its synthesis is relatively straightforward [16]. Furthermore, complexes of this substance with Ag(I) salts carrying different free ions have been reported in the literature; Reger et al.[17] used Bis(1-pyrazolyl) methane, Bonfant et al. [18] used Br, I-phenyl(bis pyrazolyl)methane, and I-alkynophenyl(bispyrazolyl) methane, Dura et al.[19] used Bis(pyrazolyl)(pyridin-3-yl) methane as ligands. L_2 is a ligand utilized in coordination chemistry studies and is commercially available. Several complexes of this ligand with Fe(II) have been reported in research [20]. This study prepared complexes with $AgNO_3$ and $AgClO_3$ in a methanol medium using L_1 and L_2 ligands. The complexes were analyzed using the single-crystal XRD method, and molecular models were determined. Furthermore, thermal degradation and thermokinetic analysis were conducted utilizing the TGA method.

The antimicrobial characteristics of Ag(I) salts and complexes are recognized globally, and research into the antimicrobial efficacy of novel materials is ongoing [21–23]. Therefore, investigations into the antimicrobial properties of these complexes, designed for use as detonators, were also conducted.

Experimental

Using general devices and characterization methods

The investigation involved the analysis of silver(I) utilizing the GBC brand Avanta PM model AAS apparatus, while the C, H, N analysis was conducted with the Eurovector 3018 C, H, N, S analyzer. FTIR spectra were obtained using the Shimadzu Infinity model FTIR spectrometer. The spectra of the ligands were obtained using ^{13}C-NMR and ^{1}H-NMR techniques on the Bruker Ultrashield 300 MHz NMR instrument. The crystal structures of complexes **I** and **II** were determined by single-crystal X-ray diffraction. Reflection data were collected at room temperature on a Bruker APEX II CCD diffractometer. Absorption correction was done by using SADABS [24]. The structures were solved by direct methods using SHELXT 2018/2 [25] and refined by full-matrix least squares on F^2 using SHELXTL-2019 [26]. Material preparation for publication is carried out by using PLATON [27], ORTEP software within WinGX [28] and Mercury 4.0 [29] programs. Thermal analyses were conducted using Shimadzu DTG 60 and DSC50 instruments. Thermal analyses were conducted in an atmosphere of nitrogen, spanning from room temperature to 500 °C, utilizing an aluminum pan as the sample holder. Thermokinetic analyses were conducted using 2, 5, 10, 15, 20, and 25 °C min^{-1} heating rates. Thermokinetic calculations were performed according to Ozawa–Flynn–Wall (OFW) [30] and Kissenger–Akahira–Sunose (KAS)[31] methods. The kinetic parameters of the complexes were calculated from thermogravimetric curves of all heating rates using temperatures corresponding to different values of g(α) (0.2–0.8). The values for activation energy and the pre-exponential factor were calculated through graphical methods, utilizing the determined temperature values by the KAS and OFW methods. The equations used in these calculations are presented as follows:

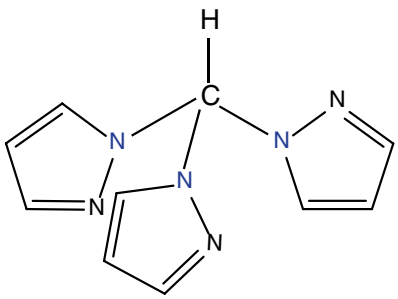

Ligand 1 (L_1)
Tris(pyrazol-1-yl) methane
$CH(C_3H_3N_2)_2$

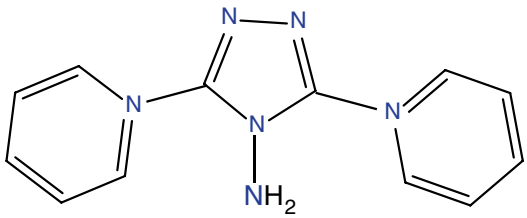

Ligand 2 (L_2)
3,5-bis(pyridin-2-yl)-4-amino-1,2,4-triazole
$C_2H_2N_4(C_5H_4N)_2$

Fig. 1 Chemical structure of ligands

Ozawa–Flynn–Wall (OFW):

$$\ln \beta = \ln\left[\frac{0.0048AE_a}{Rg(\alpha)}\right] - 1.0516\left[\frac{E_a}{RT}\right] \quad (1)$$

Kissenger–Akahira–Sunose (KAS):

$$\ln\left[\frac{\beta}{T^2}\right] = \ln\left[\frac{AE_a}{Rg(\alpha)}\right] - \left[\frac{E_a}{RT}\right] \quad (2)$$

where β is a heating speed as $^{o}C\ min^{-1}$, R universal gas constant, E_a thermal activation energy (kJ mol^{-1}), A Arrhenius pre-exponential factor, T temperature in K, $g(\alpha)$ fractional completed fraction of thermal fracture reaction. As previously stated, the equations were formulated assuming a reaction order of $n = 1$. E_a and A values were calculated from the intercept and slopes of the graphs obtained. Thermodynamic parameters in thermal decomposition could be calculated using these values [32].

$$\Delta S = 2.303\left[\log\frac{Ah}{kT}\right]R \quad (3)$$

$$\Delta H = E_a - RT \quad (4)$$

$$\Delta G = \Delta H - T\Delta S \quad (5)$$

Preparation of ligands

Ligand 1; L_1: The preparation of this ligand was carried out with the catalyst tetrabutylammonium tetrafluoroborate ($(n\text{-}C_4H_9)_4NBF_4$), utilizing chloroform ($CHCl_3$), pyrazole ($C_3H_4N_2$), and potassium carbonate (K_2CO_3), following the procedures that were found in the literature [16].

Procedure: 13.8 g (0.1 mol) of K_2CO_3 was placed in a 250-mL round-bottomed flask, to which 39.85 g (0.3 mol) of $CHCl_3$ and 3.35 g (0.05 mol) of pyrazole were added. To this mixture, 0.5 g $n\text{-}C_4H_9)_4NBF_4$ was added as a catalyst and boiled under reflux for 36 h. The initially white mixture transformed into shades of yellow and brown as time progressed. The brown liquid phase, subsequently separated from the solid K_2CO_3 through filtration, was evaporated until complete removal of $CHCl_3$ was achieved. The resulting oily residue was extracted 7–8 times with n-hexane ($n\text{-}C_6H_{14}$), followed by evaporation until the volume of $n\text{-}C_6H_{14}$ was reduced by half. The cooling process was conducted using an ice bath, separating the crystallized substance (L_1) through filtration and subsequent air drying. The ligand L_1 was recrystallized in methanol and subsequently air-dried once more.

L_1, $CH(C_3H_3N_2)_2$: Yield: 38–40%.

Melting point (m.p.):107–108 °C.

Element Analysis: Expected: C: 56.07, H: 4.70, N: 39.22%

Found: C: 55.87, H: 4.53, N: 38.75%.

^{13}CNMR data in $d_6\text{-}CH_3SOCH_3$ (δ, ppm): 141.45, 130.65, 107.42 (ring carbons), 82.05 (aliphatic carbon) (Fig. 2a).

^{1}HNMR data in $d_6\text{-}CH_3SOCH_3$ (δ, ppm): 6.42 (t) (3H), 7.67 (d) (3H), 7.90 (d), 8.99 (s) (1H). (Fig. 2b).

Important IR data (cm^{-1}): $\nu_{N\text{-}H}$:3165–3109, $\nu_{C\text{-}H(Ar)}$: 3106–3116, $\nu_{C\text{-}H(Aliph)}$:2989, $\nu_{C=N}$:1512, $\nu_{C=C}$:1384, $\nu_{C\text{-}N}$:1083, $\delta_{C\text{-}H(Ar)}$: 750. (Fig. 2c).

MS m/z: 214 $[M]^+$ (Basepeak), 147 $[CH(C_3H_3N_2)_2]^+$, 148 $[CH(C_3H_4N_2)_2]^+$, 120 $[(C_3H_3N_2)_2CH=CH=CN]^+$, 92 $[CH=N\text{-}C_3H_3N_2]^+$, 91 $[CH=N\text{-}C_3H_2N_2]^+$, 52 $[CH=CH\text{-}C=N]^+$.

Ligand II, L_2, was obtained from Sigma–Aldrich (CAS No: 1671–88-1).

Important IR data (cm^{-1}): $\nu_{N\text{-}H}$:3292 (-NH_2)- 3213 (N-H_{ring}) $\nu_{C\text{-}H(Ar)}$: 3094–3197, $\nu_{C=C(ring)}$: 1588, $\delta_{C\text{-}H(Ar)}$: 786 cm^{-1} (Fig S1).

Preparation of complexes

Complex I; $[AgCH(C_3H_3N_2)_3.\ ClO_3]$: $AgClO_3$ is not commercially available; therefore, this material was prepared using $AgNO_3$ according to methods in the literature [33]. 0.428 g (0.002 mol) of Tris(pyrazole-1-yl) methane was dissolved in 30 mL of heated methanol within a 250 mL beaker. A solution of 0.383 g (0.002 mol) $AgClO_3$ was added to this solution, dissolved in 40 mL of hot methanol. The solution was allowed to rest for a duration of one day, following which the resulting white crystalline precipitate was subjected to filtration and subsequently air-dried.

$C_{10}H_{10}N_6ClO_3Ag$: Yield 50–52%.

Element Analysis: Expected: C: 29.62, H: 2.48, N: 20.71, Ag: 26.60%.

Found: C: 28.87, H: 2.55, N: 19.95, Ag: 26.52 %.

Important IR data (cm^{-1}): $\nu_{N\text{-}H}$:3134, $\nu_{C\text{-}H(Ar)}$: 3104–3116, $\nu_{C\text{-}H(Aliph)}$:2988, $\nu_{C=C(ring)}$:1523, $\nu_{Cl\text{-}O}$: 916, $\delta_{C\text{-}H(Ar)}$: 744. (Fig. 3a).

Complex II; $[AgC_2H_2N_4(C_5H_4N)_2]\ NO_3$: 0.477 g (0.002 mol) 3,5-bis(pyridin-2-yl)-4-amino-1,2,4-triazole was weighed and dissolved in 40 mL of heated methanol within a 150 mL beaker. A solution of 0.340 g (0.002 mol) $AgNO_3$ was added to this solution, dissolved in 40 mL of hot methanol. The solution was allowed to rest for a duration of one day, following which the resulting white crystalline precipitate was subjected to filtration and subsequently air-dried.

$C_{12}H_{10}N_7O_3Ag$: Yield 55–60%.

Element Analysis: Expected: C: 35.32, H: 2.46, N: 24.01, Ag: 26.43%.

Found: C: 35.41, H: 2.53, N: 23.37, Ag: 25.82 %.

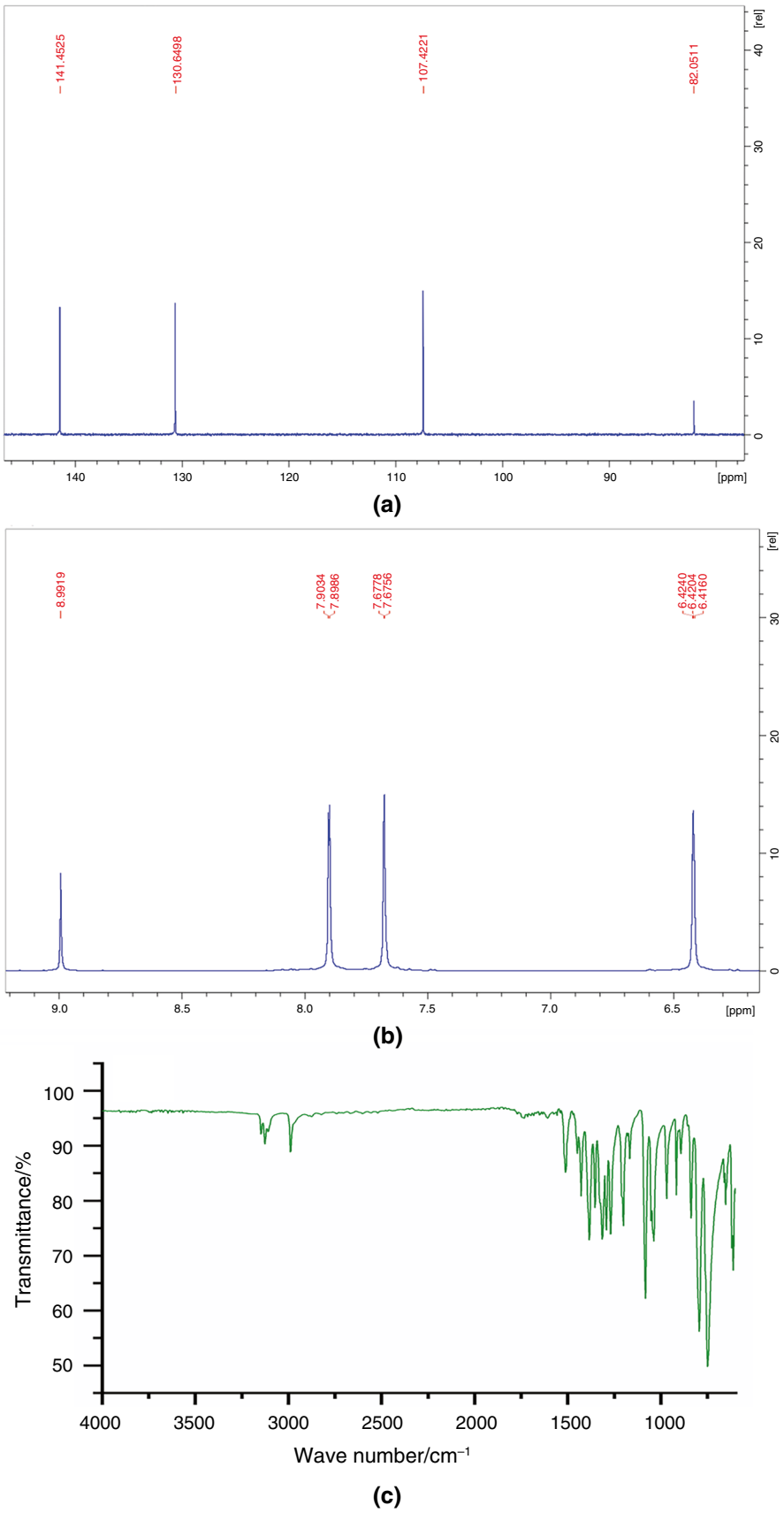

Fig. 2 **a** ^{13}CNMR spectrum, **b** ^{1}HNMR spectrum, and **c** FTIR spectrum of L_1

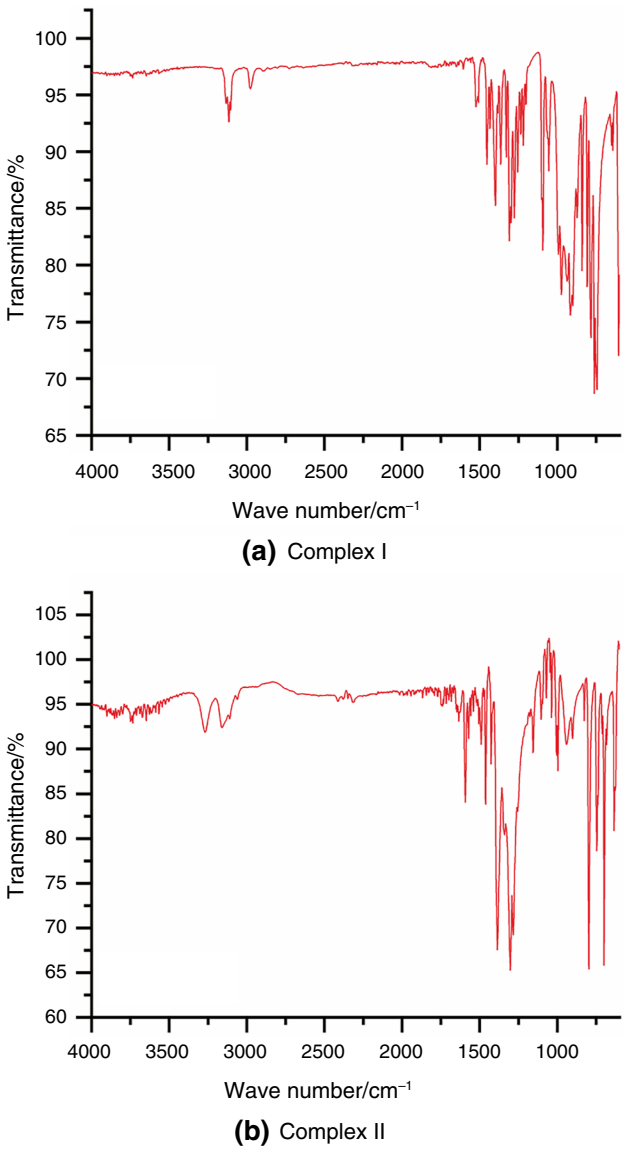

Fig. 3 FTIR spectra of (a) Complex I and (b) Complex II

Important IR data (cm^{-1}): $\nu_{N\text{-}H}$:3259 (-NH_2)- 2271 (N-H_{ring}) $\nu_{C\text{-}H(Ar)}$: 3094–3115, $\nu_{C=C(ring)}$:1597, $\nu_{N=O}$:962, $\delta_{C\text{-}H(Ar)}$: 734. (Fig. 3b).

Biological activity of the complexes

Strains and culture conditions

The list of microbial strains preferred in the minimum inhibitory concentration (MIC) test is shown in Table 1.

The strains were stored at – 86 °C with 60% glycerol. The culture strains were first inoculated onto Tryptic Soy Agar plates (TSA; Merck, Darmstadt, Germany). The plates were then incubated overnight at 37 ℃. After incubation, individual colonies were picked from each culture using sterile loops and inoculated onto Mueller–Hinton Agar plates (MHA; Merck, Darmstadt, Germany). These culture plates were used for the minimum inhibitory concentration test.

Table 1 List of the strains

Microorganisms	Gram reaction
Staphylococcus aureus ATCC 25923	Gram-positive
Methicillin-resistant *S. aureus* ATCC 43300	Gram-positive
Bacillus subtilis ATCC 6633	Gram-positive
Enterococcus faecalis ATCC 29212	Gram-positive
Pseudomonas aeruginosa ATCC 27853	Gram-negative
Salmonella Typhimurium ATCC 13311	Gram-negative
Escherichia coli ATCC 25922	Gram-negative
Candida albicans ATCC 26555	Fungal strain

Minimum inhibitory concentration (MIC) test

The MIC values for the strains susceptible to complexes **I** and **II** were determined according to the recommendations of the CLSI (Clinical & Laboratory Standards Institute)[34]. Active cultures were prepared as described above. Single colonies were taken from each culture and suspended in physiological saline (0.9% NaCl) to set the 0.5 McFarland standard. First, 100 µL of Mueller Hinton Broth (MHB; Merck, Darmstadt, Germany) medium was added to each well of the microdilution plates using a multichannel micropipette. Then a series of dilutions with 2500 µg mL^{-1} stock concentrations of complexes **I** and **II** were prepared using the microdilution method. The stock solutions were prepared in 10% DMSO (dimethyl sulfoxide), which has no antimicrobial effect against the test strains. The wells containing only the medium and inoculum were designed as positive control wells, and the wells containing only the medium were designed as negative control wells.

The microdilution plates were incubated at 37 °C for 18 h. The concentration values of the first wells, in which no microbial growth was observed at the end of the incubation, were considered as MIC values.

Antibiofilm activity

The strains *P. aeruginosa* ATCC 27853 and *S. aureus* ATCC 25923 were used for the biofilm studies as they serve as significant Gram-negative and Gram-positive models, respectively. Specific incubation conditions and modified media were preferred for each strain to promote biofilm formation. *P. aeruginosa* ATCC 27853 strain was cultured in Tryptic Soy Broth (TSB) medium with 1% glucose, while *S. aureus* ATCC 25923 strain was cultured in TSB medium with 3% NaCl, according to Onbas et al. [35]. The active

cultures of each strain were prepared according to the above instructions.

Single colonies of each strain were taken from the cultures and inoculated into appropriate media (5 mL). Broth cultures were incubated overnight at 37 °C. After incubation, the active cultures of each strain were diluted 1:100 in the appropriate media. After the suspensions were prepared, 140 µL of the modified media were added to the wells of the 96-well U-bottom microtiter plates (LP Italiana, Italy). At this point, a serial dilution was performed for each strain taking into account the previously determined MIC values (twofold, MIC, MIC/2, MIC/4, MIC/8, MIC/16…). 10 µL of each culture suspension was added to the wells of the microtiter plates. The wells containing only media and inoculum served as positive controls, while the wells containing only media served as negative controls.

The plates were incubated under static conditions at 37 °C for 24 h. At the end of the incubation, a crystal violet binding assay was performed according to the method of Onbas et al. [35]. The dissolved crystal violet dye was read in a microplate reader set to 595 nm (BioTek Elisa reader, µQuant, Biotek Inc., Winooski, VT, USA).

Statistical analysis

Data are presented as means and standard deviations. Multiple comparisons were performed using the One-Way ANOVA test, and Tukey's test was used for post-hoc comparisons. All analyses were performed using GraphPad software (version 8.0, Boston, MA, USA).

Results

FTIR analysis

The overlaid FTIR spectra of the complex and ligands are illustrated in Figs. S2 and S3. In Fig. S2, the $\nu_{Cl\text{-}O}$ stretches expected at 977–1032–1109 cm^{-1} in the IR spectrum of $NaClO_3$ as reported in the literatüre [36] are observed to be shifted to 900–916–976 cm^{-1} in complex **I**. This indicates that ClO_3^- coordinates to L_1 through its oxygen atom. In Fig. S3, the $\nu_{N\text{-}H}$ stretches observed at 3292 cm^{-1} in L_2 shifted to 3269 cm^{-1} in Complex **II**. This shift is due to the coordination of nitrogen donors to the Ag(I) ion or hydrogen bonds. Also, there was no noticeable change in the $\nu_{C=C(ring)}$, $\delta_{C\text{-}H(Ar)}$ stretching vibrations, and $\nu_{N=O}$ signals. In the literature, signals at 1303, 1348, and 1380 cm^{-1} have been reported for ionic nitrate in the IR spectra of $AgNO_3$ and $NaNO_3$ salts [37, 38]**.** Therefore, the strong $\nu_{N=O}$ stretching observed at 1340 cm^{-1} in the FTIR spectrum (Fig. S3) of complex **II** can be attributed to ionic NO_3^-. The analysis via single-crystal XRD further confirmed that NO_3^- exists in an uncoordinated state, maintaining its ionic character.

XRD analysis

X-ray powder diffraction (XRPD) patterns of complexes **I** and **II** are presented in Figs. S4 and S5. The theoretical and experimental XRPD patterns of the complexes exhibited significant levels of overlap. Sharp and clear peaks provide information about the crystal structure; the peaks broaden as the crystal size lowers. [39]. The fact that the experimental pattern in complex **II** is wider than the theoretical pattern can be attributed to the presence of microstrains in the crystal structure. Furthermore, certain additional peaks detected in the experimental patterns could be explained by the presence of impurities.

The $\mathbf{L_1}$ ligand, characterized by six nitrogen donor atoms and three coordination sites, is a commonly referenced NNN-type ligand in research [16]. Despite the presence of six nitrogen atoms in the structure of the L_2 ligand, it exhibits the ability to operate as either a two- or three-dentate ligand. The molecular models of the two complexes obtained from single-crystal XRD analyses were constructed using the Pluton/Ortep program and are illustrated in Figs. 4 and 5, respectively. Crystallographic data collection and refinement details of complexes **I** and **II** are given in Table 2. As seen in Fig. 4, two of the N donors on the three pyrazole rings in the L_1 ligand in the complex **I** coordinated an Ag(Ag2) ion. The third nitrogen in the structure (L_1) formed a bridge and coordinated the second Ag(Ag1) ion. In contrast, two of the three nitrogen donors from the second ligand coordinate with the Ag1 ion, whereas the third nitrogen donor of this ligand once more facilitates coordination with the Ag1

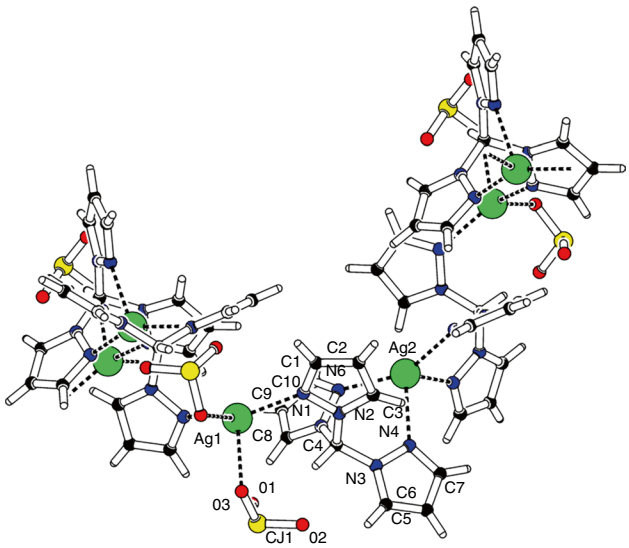

Fig. 4 Molecular model of complex **I** created by the Pluton program

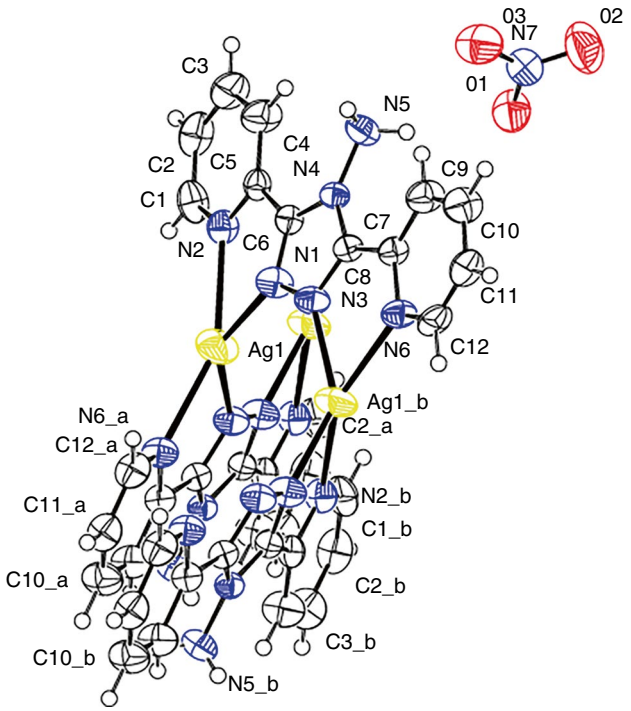

Fig. 5 ORTEP drawing of complex **II**

ion through a bridge. The two oxygens of the chlorate ion, which serve as the free ion, coordinate with the Ag1 ion. In this case, the coordination environment surrounding the Ag1 ion is characterized by AgN_2O_2, whereas the Ag2 ion has a coordination sphere of AgN_4. Consequently, a dinuclear complex **I** that included distinct circumferences of the two central atoms was synthesized.

Figure 5 depicts complex **II**, which is also dinuclear, but the coordination of the two Ag(I) ions remains identical. Two nitrogen donors from the first ligand coordinate with the Ag1 ion, while the remaining two nitrogen donors interact with the Ag2 ion through the bridge. Consequently, a coordination sphere of AgN_4 is established around each of the Ag(I) ions. As a result, complex **I** exhibits non-symmetrical characteristics as a dinuclear complex, whereas complex **II** is designated as a dinuclear complex.

The coordination sphere of silver ions in both complexes exhibits a highly deformed tetrahedral arrangement. Recent studies have indicated that Ag(I) ions generate degraded tetrahedral complexes when interacting with various polydentate ligands [11, 18, 19, 40, 41]; however, the degree of degradation is major. The significant bond lengths and angles measured around the coordination sphere in the complexes are given in Table 3.

The analysis of the angles presented in Table 3 reveals that the coordination sphere surrounding the Ag(I) ions in both complexes **I** and **II** exhibits a deformed tetrahedral configuration. As previously highlighted, the coordination sphere consists of AgN_2O_2 in complex **I** and AgN_4 in complex **II.** The internal angles of the tetrahedron, which are expected to be 109°, were recorded as 94.6, 136.3(3), 151.2(3), and 82.74(19)° in complex **I**, while in complex **II**, they were measured at 142.3, 154.6, 70.1, and 69.2°. These angles show that the distortion is exceptionally high. In the study by Qin et al., the complex was obtained with the L_2 ligand, Ag(I) ion, and CF_3-SO_3^- free ion [42]. The study's tetrahedron internal angles were 130.70, 146.11, 71.56°. Furthermore, given that the free ion is CF_3-SO_3^-, one cannot anticipate the presence of explosive characteristics in this complex.

In complex **II**, the internal angles of the tetrahedral coordination exhibit relatively small values of 70.1° and 69.2°, whereas in complex **I**, such small angles are absent at this level. This occurs due to the involvement of one of the oxygen atoms from the ClO_3^- free ion in coordinating complex **I**. This ion exhibits greater geometric freedom, resulting in the angles of the tetrahedron within the complex being slightly nearer to the ideal configuration.

Thermal analysis

The variations in coordination influence the chemical characteristics of complexes. The TG and DTA curves of the complexes, as shown in Figs. 6 and 7, were recorded over a temperature range from room to 500 °C.

Complex **I** (Fig. 6) starts to decompose exothermically at approximately 200 °C. This decomposition accelerates at around 245 °C, and after this temperature, beyond which the molecule undergoes a swift exothermic decomposition. Analysis of the TG and DTA curves for complex **I** indicated that thermal decomposition occurs in two steps.

Complex **II** gives entirely different TG and DTA curves (Fig. 7). Stable up to 214 °C, the complex suddenly decomposes within a narrow temperature range of approximately 0.2 °C, resulting in a rapid exothermic reaction leading to the complete mass loss. The phenomenon is rare in explosive materials. The complex remains stable until it reaches a specific temperature, at this point, the entire substance transitions into a gaseous phase through a strong exothermic process. The characteristics of complex **II** indicate its potential application as an initial explosive [15].

Both complexes' TG and DTA curves exhibit irregularities in the regions where swift reactions occur. Complex I showed a mass loss of around 55% after the 1st and 2nd thermal decompositions (Fig. 8a). Similarly, in complex **II**, the sudden mass loss observed in the 200–300 C range indicates that the complex undergoes thermal decomposition (Fig. 9a). The nature of the gaseous products resulting from thermal decomposition can differ based on the atmosphere during TG analysis. Removing the gaseous products causes a loss of mass as well as a brief decline in pan temperature.

Table 2 Crystallographic data of complexes **I** and **II**

Parameters	Complexes	
	Complex I	Complex II
Empirical formula	$C_{10}H_{10}O_3N_6ClAg$	$C_{12}H_{10}O_3N_7Ag$
Formula weight	405.56	408.14
Temperature (K)	293(2)	293(2)
Wavelength (Å) MoKα	0.71073	0.71073
Crystal system	Orthorhombic	Orthorhombic
Space group	$C222_1$	$P2_12_12_1$
a (Å)	10.0511(10)	7.468(2)
b (Å)	9.144(2)	8.162(3)
c (Å)	14.8243(15)	22.808(7)
$\alpha=\gamma=\beta$ (°)	90	90
V (Å^3)	2852.5(5)	1390.1(7)
Z	8	4
Dc/g.cm^{-3}	1.889	1.950
μ/mm^{-1}	1.619	1.479
F(000)	1600	808
Crystal description/color	Plate/colorless	Plate/colorless
Crystal size/mm	0.207 × 0.193 × 0.096	0.289 × 0.103 × 0.094
Θ range for data collection (°)	2.128–25.242	1.786–26.997
Measured ref./R_{int}	11,072/0.0479	20,185/0.1167
Independent/[I > 2σ(I)] ref	2628/2370	3037/2235
No. of parameters	192	212
Final R_1, wR_2 indices [$I>2\sigma(I)$]	0.0325/0.0781	0.0449/0.0989
R_1, wR_2 indices (all data)	0.0379/0.0813	0.0719/0.1109
Goodness-of-fit on F^2	0.984	0.997
$\Delta\rho_{max,}$ $\Delta\rho_{min}$/e Å^{-3}	0.719/−0.964	0.755/−0.662
CCDC number	2,379,785	2,379,784

This can be observed as a deformation in the TG and DTA curves. The 3D plotted TG and DTA curves of complexes **I** and **II** distinctly illustrate this phenomenon (Figs. 8 and 9).

The complex **I** has a two-step mass loss, as observed from the TG and DTA curves and a corresponding DTA curve (Table 4). In contrast, complex **II** shows a considerable mass loss in a very narrow temperature range at a heating rate of 10 °C min^{-1}. In complex **II**, the pan exhibits no residue, whereas complex **I** shows approximately 55% residue present. Initially, this residue was considered Ag_2O, but the ratio of Ag_2O residue to molecular mass is 27.64%. In this case, the mass loss should have been 72.36%. The residue resulting from the thermal decomposition of complex **I** was considered another substance, and TG–DTA analysis of the complex was performed in an O_2 atmosphere (Fig. 10). As illustrated in Fig. 9a, the observed mass loss was approximately 65.59 ± 1.91%, leaving a residual mass of 35%. Assuming that the residue is AgCl, a theoretical mass loss of 65.82% is expected. The findings indicate that the final product of the decomposition reaction in complex **I** is AgCl. Research indicates that chlorate salts undergo decomposition at approximately 170 °C, releasing O_2, while the chloride compound of the cation remains (AgCl) [9]. In complex **I**, the initial phase involves releasing O_2, which subsequently oxidizes around 22% of the organic ligand's mass, removing it from the environment (Fig. 10). The remaining residue decays with increasing temperature after this temperature.

Thermokinetic analysis was performed using TG curves of complexes **I** and **II**. The thermokinetic data (activation energies, E_a, and Arrhenius exponential factor, A) of the thermal decompositions were calculated by the Ozawa-Flynn-Wall (OFW) and Kissinger–Akahira–Sunose (KAS) methods. This analysis was conducted separately for the two steps of complex **I** and as a single step for complex **II** [43–45]. These results were used to calculate the thermodynamic parameters of the thermal decompositions. The calculated thermokinetic data and thermodynamic parameters are given in Tables 5 and 6, respectively.

The focus here is on the reason for this significant difference between the thermal decomposition reactions of the two complexes. The thermal decomposition of complex **I** occurred in two steps, while complex **II** occurred in one step with a swift reaction. The ClO_3^- ion is a stronger oxidant than the NO_3^- ion, and one would expect a faster decomposition

Table 3 Selected bond lengths and angles around the coordination sphere

Complex	Bond lengths/Å	Bond angles/°
		N1 Ag1 N1 136.3(3)
	Ag1 N1 2.262(5)	N4 Ag2 N4 94.6(3)
	Ag1 N1 2.262(5)	N6 Ag2 N4 117.6(2)
	Ag2 N4 2.409(6)	N6 Ag2 N4 117.6(2)
	Ag2 N4 2.409(6)	N6 Ag2 N4 82.74(19)
	Ag2 N6 2.230(5)	N6 Ag2 N4 82.74(19)
	Ag2 N6 2.230(5)	N6 Ag2 N6 151.2(3)
		N2 N1 Ag1 127.7(4)
I		C1 N1 Ag1 124.6(4)
		C1 N1 N2 104.1(5)
		N1 N2 C4 117.2(4)
		C3 N2 N1 111.6(5)
		C3 N2 C4 130.4(5)
		N4 N3 C4 121.5(5)
		C5 N3 N4 110.9(5)
		C5 N3 C4 127.5(5)
		N3 N4 Ag2 121.3(4)
		C7 N4 Ag2 133.7(5)
		C7 N4 N3 105.0(6)
	Ag1 N1 2.228(6)	N1 Ag1 N2 69.2(2)
	Ag1 N2 2.499(6)	N1 Ag1 N3 142.3(2)
	Ag1 N3 2.260(6)	N1 Ag1 N6 126.0(2)
	Ag1 N6 2.429(6)	N3 Ag1 N2 111.5(2)
		N3 Ag1 N6 70.1(2)
		N6 Ag1 N2 154.6(2)
II		N3 N1 Ag1 130.1(5)
		C6 N1 Ag1 120.4(5)
		C6 N1 N3 107.7(6)
		C1 N2 Ag1 126.6(6)
		C1 N2 C5 118.2(7)
		C5 N2 Ag1 115.1(4)
		N1 N3 Ag1 131.9(5)
		C7 N3 Ag1 118.4(5)

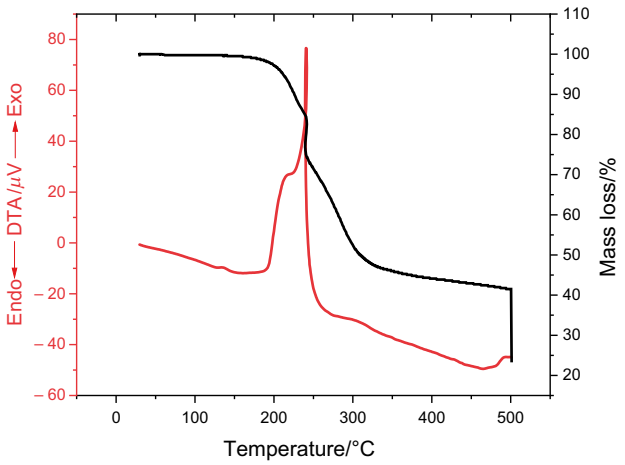

Fig. 6 TG (black) and DTA (red) curves of complex **I**

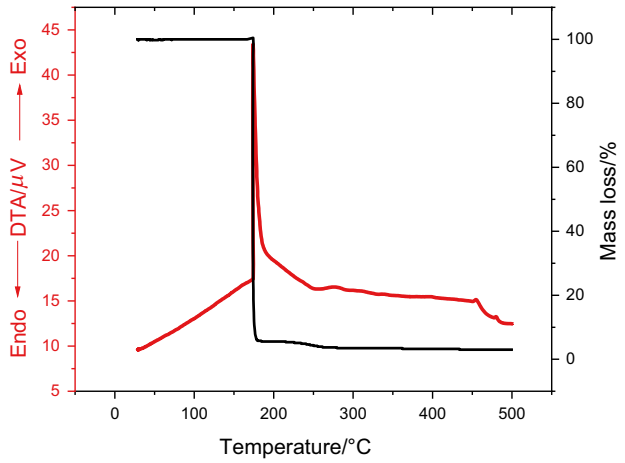

Fig. 7 TG (black) and DTA (red) curves of complex **II**

of complex **I**, but the opposite was observed. The reason for this is undoubtedly the coordination in complexes and the intramolecular or intermolecular interactions caused by this coordination. Upon analyzing the hydrogen bonds with the Platon program (Table 7), a strong intermolecular interaction is not detected in complex **I** [46]. On the other hand, strong intermolecular hydrogen bonding occurs in complex **II**. The hydrogen bonds obtained from the Platon program for the two complexes are detailed in Table 7. Also, the potential hydrogen bonding interactions within the complexes were illustrated using Mercury software (Fig. 11).

Table 7 indicates that no notable intramolecular and intermolecular hydrogen bonding interactions are present in complex **I**. Many C-H…..X (X = O or N) interactions are noted, yet these interactions do not represent conventional hydrogen bonding. In certain investigations, these have been identified as hydrogen bonds [47]. These interactions were found using crystallographic programs with the distance between atoms as a reference. They are not interactions that fit the classical definition of hydrogen bonding [48]. Complex **II** exhibits two strong hydrogen bonding interactions, as illustrated in Fig. 11; these hydrogen bonds are formed between the -NH_2 group of the ligand and the ionic NO_3^- ion. The presence of hydrogen bonds increases the thermal stability of energetic compounds [15]. As a result, the difference between the thermal behavior of the two complexes is primarily due to the stability imparted by hydrogen bonds and secondarily to the initiation of thermal decomposition of the ClO_3^- ion.

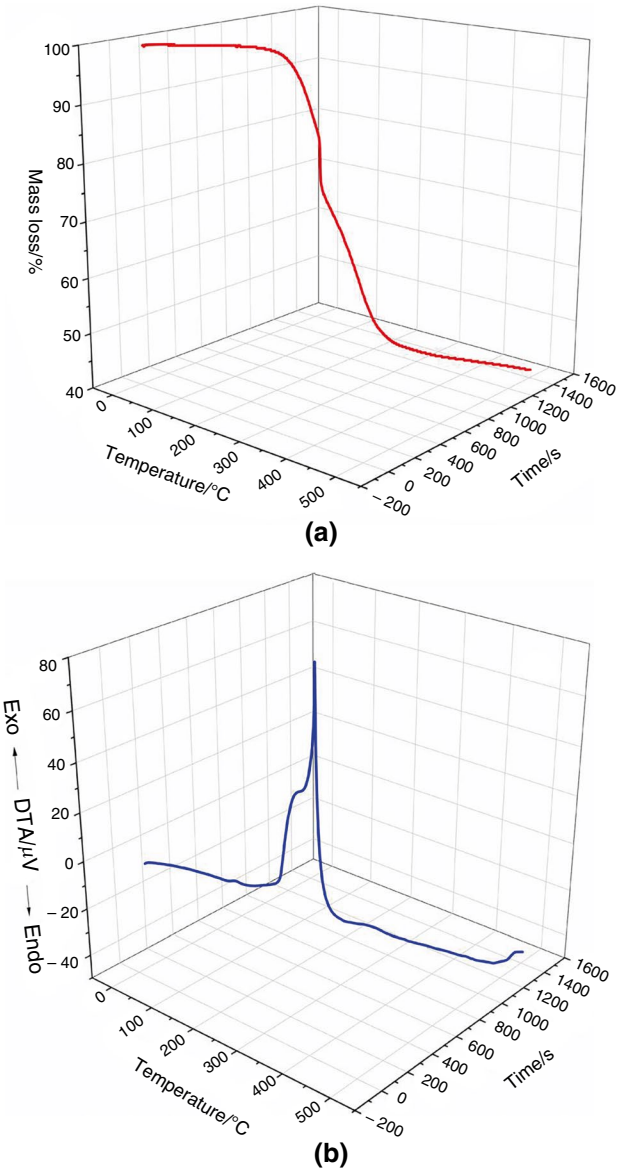

Fig. 8 3D plotted (a) TG and (b) DTA curves of complex **I**

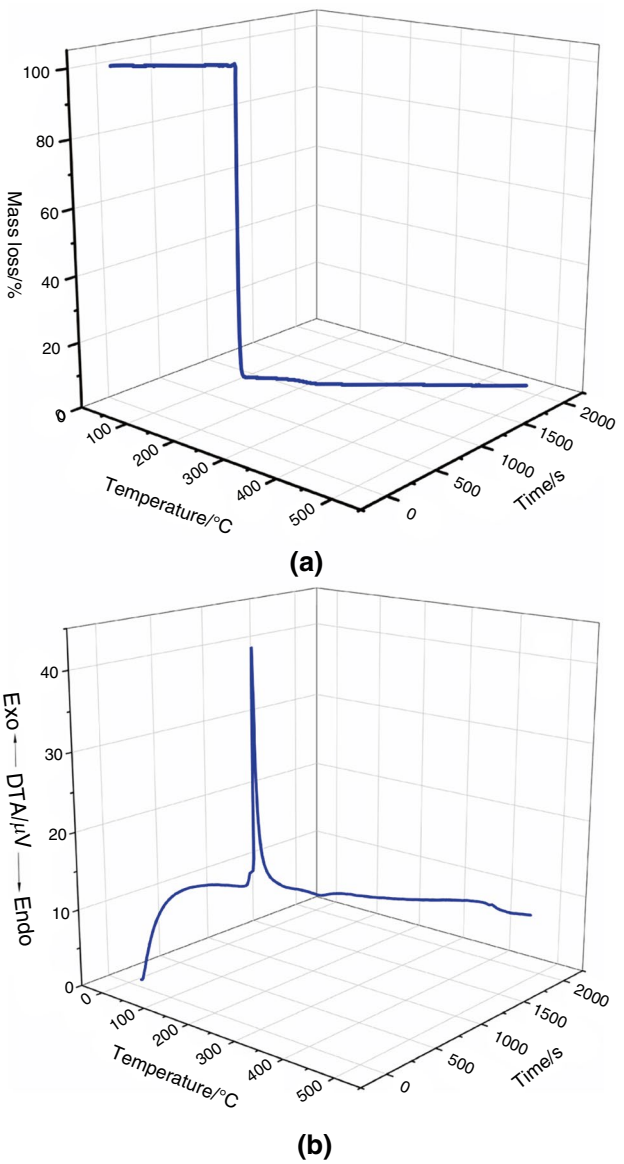

Fig. 9 3D plotted (a) TG and (b) DTA curves of complex **II**

Minimum inhibitory concentration (MIC) test

The MIC values are listed in Table 8. The concentrations of complexes **I** and **II** ranged between 0 and 1250 μg mL^{-1}. All microbial strains tested were susceptible to complexes **I** and **II**. Complex **I** proved to be more effective as it showed antimicrobial activity against all strains at lower concentrations. *B. subtilis* ATCC 6633 was found to be the most susceptible strain, and the concentration values of complexes **I** and **II** were calculated to be 2.44 and 4.88 μg mL^{-1},

Table 4 Thermoanalytical data of the complexes

Complexes	1th Thermal Decomposition		2nd Thermal Decomposition	
	Temperature range/°C	Mass loss /%	Temperature range/°C	Mass loss/%
I	190–215	22.65 ± 0.69	215–243	34.26 ± 2.61
II	169–170	94.45 ± 0.84	–	–

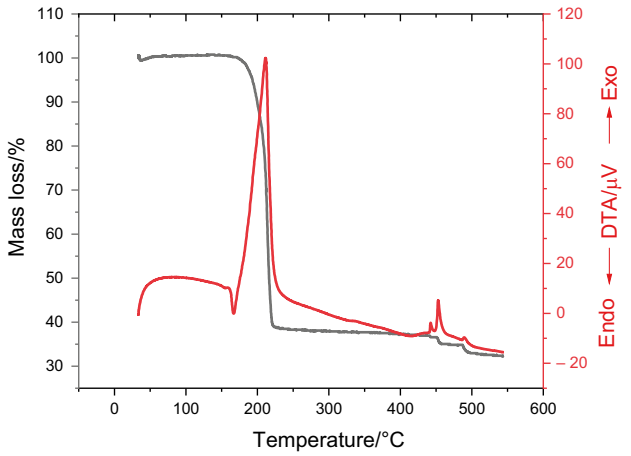

Fig. 10 TG–DTA curves of complex **I** in O_2 atmosphere

respectively. The lowest MIC values were determined for complex **II** with 78.13 μg mL^{-1} for the strains *S. aureus* ATCC 25923, *E. faecalis* ATCC 29212, *E. coli* ATCC 25922, and *C. albicans* ATCC 26555. According to this result, both complexes **I** and **II** also showed antifungal effects.

Antibiofilm activity

The inhibitory effects of complexes **I** and **II** on biofilm formation were investigated using a crystal violet test against *S. aureus* ATCC 25923 and *P. aeruginosa* ATCC 27853. Subinhibitory concentrations, expressed as fractions of the MIC of each compound (e.g., MIC/2 to MIC/512), were applied during biofilm formation to evaluate their preventive effect.

Both complexes significantly inhibited biofilm formation in both strains, albeit with different efficacy. Complex **I** showed a stronger inhibitory effect against *S. aureus* ATCC 25923 compared to complex **II**. Complex **I** significantly reduced biofilm formation at concentrations up to MIC/64 (19.53 μg $mL^{-1} \div 64$), while complex **II** (MIC: 78.13 μg mL^{-1}) required at least MIC/16 for comparable effects. This indicates a higher sensitivity of *S. aureus* biofilm formation to complex **I** at lower doses (Fig. 12a).

In contrast, complex **II** was more effective against *P. aeruginosa* ATCC 27853. Significant inhibition was observed at all sub-MIC levels tested down to MIC/64,

Table 5 Thermokinetic analysis results of complexes

Complexes	Measuring and calculation methods			
	KAS		OFW	
	E_a/kJ mol^{-1}	A/min^{-1}	E_a/kJ mol^{-1}	A/min^{-1}
Complex **I** 1th thermal decomposition	102.64 ± 10.78	30.46	105.4 ± 10.3	1.12×10^{10}
2nd thermal decomposition	85.013 ± 7.328	0.298	89.372 ± 6.642	1.27×10^{8}
Complex **II**	134.4 ± 11.5	2.85×10^{6}	134.8 ± 10.9	7.07×10^{15}

Table 6 The calculated thermodynamic parameters of complexes

Complexes	Methods					
	KAS			OFW		
	ΔH/kJ mol^{-1}	ΔS/J K^{-1}	ΔG/kJ mol^{-1}	ΔH/kJ mol^{-1}	ΔS/J K^{-1}	ΔG/kJ mol^{-1}
Complex **I** 1th thermal decomposition	100.96	− 220.84	211.41	103.73	− 56.84	132.54
2nd thermal decomposition	83.334	− 259.31	213.02	87.694	− 94.088	134.75
Complex **II**	132.72	− 22.30	143.87	133.10	157.58	54.28

Table 7 H bonds and interactions in complexes

Complex	Donor	Acceptor	D–H	H—A	D–A	D–H–A
Complex **I**	C2–H2	O3	0.93	2.53	3.457(11)	171
	C3–H3	N4	0.93	2.59	3.041(9)	110
	C4–H4	O1	0.98	2.37	3.298(9)	158
	C4–H4	O2	0.98	2.52	3.366(10)	144
	C5–H5	O2	0.93	2.48	3.230(11)	138
	C7–H7	O1	0.93	2.47	3.392(11)	170
	C8–H8	O1	0.93	2.52	3.250(11)	136
	C10–H10	O3	0.93	2.59	3.411(11)	147
Complex **II**	N5–H5A	O1	0.87	2.12	2.966(10)	164
	N5–H5B	O1	0.87	2.12	2.966(10)	164
	C3–H3	O1	0.93	2.59	3.384(11)	158
	C4–H4	N5	0.93	2.40	3.009(11)	123
	C9–H9	O3	0.93	2.59	3.425(10)	150
	C9–H9	N5	0.93	2.57	3.187(11)	124
	C11–H11	O3	0.93	2.40	3.162(11)	139

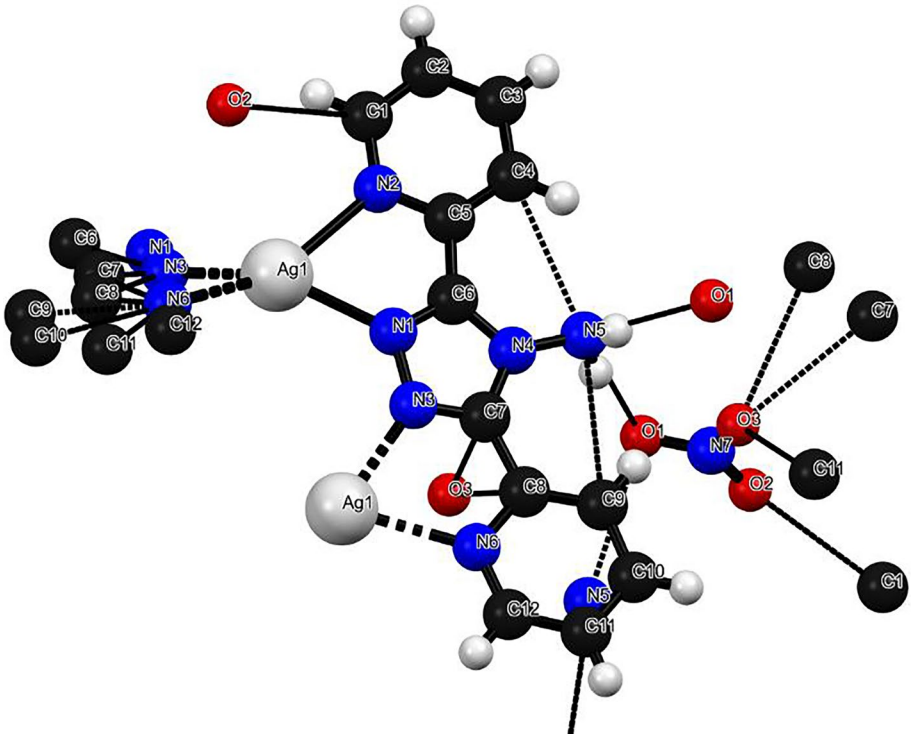

Fig. 11 Possible hydrogen bonds drawn with Mercury software

while complex **I** only produced statistically significant reductions at MIC/16 and higher. Remarkably, complex **II** maintained its antibiofilm efficacy even at highly diluted concentrations (MIC/64), indicating its strong antibiofilm potential against *P. aeruginosa* ATCC 27853 (Fig. 12 b).

These results indicate that both drugs can inhibit biofilm formation at concentrations far below their minimum inhibitory concentrations without causing cell death.

Conclusion

Two newly synthesized and extensively studied nitrogen-rich Ag(I) complexes were the focus of this investigation. Complexes **I** and **II** stand out structurally due to the extremely deformed tetrahedral coordination environments that were revealed by the single-crystal X-ray diffraction study. Distinct variations in breakdown tendencies were revealed by thermal studies. Complex II showed promise

Table 8 MIC values for the tested strains

	S. aureus ATCC 25923		Methicillin-resistant *S. aureus* ATCC 43300		*B. subtilis* ATCC 6633		*E. faecalis* ATCC 29212		*P. aeruginosa* ATCC 27853		*S.* Typhimurium ATCC 13311		*E. coli* ATCC 25922		*C. albicans* ATCC 26555	
µg/mL	I	II	I	II	I	II	I	II	I	II	I	II	I	II	I	II
1250	-	-	-	-	-	-	-	-	-	-	-	-	-	-	-	-
625	-	-	-	-	-	-	-	-	-	-	-	-	-	-	-	-
312.50	-	-	-	-	-	-	-	-	-	-	-	-	-	-	-	-
156.25	-	-	-	-	-	-	-	-	-	-	-	-	-	-	-	-
78.13	-	⊖	-	-	-	-	-	⊖	-	-	-	-	-	⊖	-	⊖
39.06	-	+	-	⊖	-	-	-	+	-	⊖	-	⊖	-	+	-	+
19.53	⊖	+	⊖	+	-	-	-	+	-	+	-	+	⊖	+	⊖	+
9.77	+	+	+	+	-	-	⊖	+	-	+	-	+	+	+	+	+
4.88	+	+	+	+	-	⊖	+	+	⊖	+	-	+	+	+	+	+
2.44	+	+	+	+	⊖	+	+	+	+	+	⊖	+	+	+	+	+
1.22	+	+	+	+	+	+	+	+	+	+	+	+	+	+	+	+

The concentration values marked with black circles represent the determined MIC values. The minimum inhibitory concentration (MIC) is defined as the lowest concentration at which no visible microbial growth is observed. Conversely, the concentrations at which microbial growth is observed are labeled with a "+" symbol

I: Complex **I**; II: Complex **II**

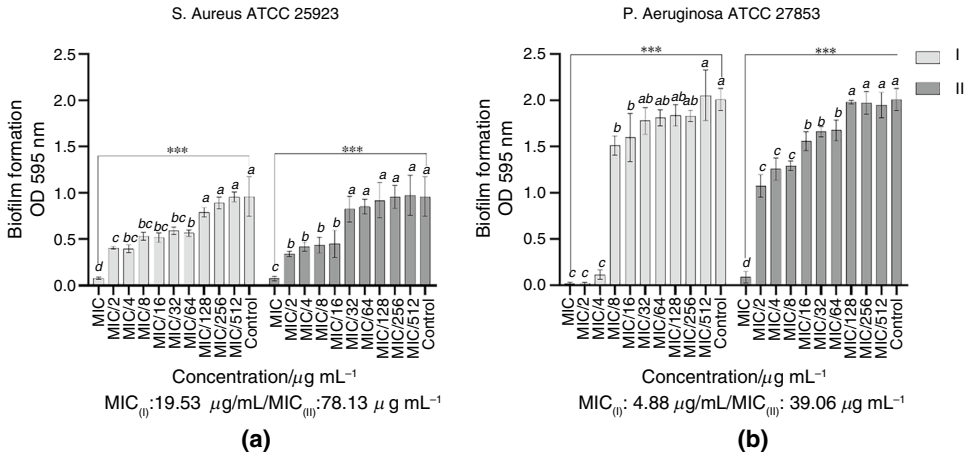

Fig. 12 Biofilm-inhibitory activity of complex **I** (light gry bars) and complex **II** (dark gray bars) against *S. aureus* ATCC 25923 **a** and *P. aeruginosa* ATCC 27853 **b**. The effects of subinhibitory concentrations, expressed as fractions of the MIC of each compound (e.g., MIC/2, MIC/4, …, MIC/512), on biofilm formation were investigated. These concentrations were applied during biofilm formation. The bars represent the mean values of three independent experiments ± standard deviation (SD). Statistical significance was determined using one-way ANOVA followed by Tukey's post-hoc test. Different lowercase letters (e.g., a, b, c) above the bars indicate statistically different groups. *$p < 0.05$, **$p < 0.01$, ***$p < 0.001$

as an effective initiator for energy applications due to its extremely fast exothermic reaction within a small temperature range. In addition, these complexes have proven effective against a range of microbes in antimicrobial investigations. The results demonstrate how the thermal stability and reactivity of Ag(I) complexes are controlled by the ligand selection and coordination interactions. Future research into the practical applications of energetic metal complexes can build on this study's important contributions to our understanding of their design and behavior.

Supplementary Information The online version contains supplementary material available at https://doi.org/10.1007/s10973-025-14430-2.

Funding Open access funding provided by the Scientific and Technological Research Council of Türkiye (TÜBİTAK).

Open Access This article is licensed under a Creative Commons Attribution 4.0 International License, which permits use, sharing, adaptation, distribution and reproduction in any medium or format, as long as you give appropriate credit to the original author(s) and the source, provide a link to the Creative Commons licence, and indicate if changes were made. The images or other third party material in this article are

included in the article's Creative Commons licence, unless indicated otherwise in a credit line to the material. If material is not included in the article's Creative Commons licence and your intended use is not permitted by statutory regulation or exceeds the permitted use, you will need to obtain permission directly from the copyright holder. To view a copy of this licence, visit http://creativecommons.org/licenses/by/4.0/.

References

1. Lommel M, Schirra R, Klapötke TM, Stierstorfer J. On the further development of silver nitrotetrazolate for practical use as a primary explosive. Propellants Explos Pyrotech. 2025;50:1–9.
2. Ji H, Liu L, Sun Q, Li X, Lu M. First structural characterization of solvate-free silver 5-nitrotetrazolate and its comparison with other energetic silver compounds in structure and property. Propellants, Explos Pyrotech. 2019;44:803–6.
3. Rodzevich AP, Kuzmina LV, Gazenauer EG, Krasheninin VI, Sozinov DY, Mamadaliev RA. The effect of additionally introduced impurities of Fe and Pb ions on silver azide decomposition. Key Eng Mater. 2017;736:101–4.
4. Wentrup C. Fulminating gold and silver. Angew Chemie Int Ed. 2019;58:14800–8.
5. Beck W. The first chemical achievements and publications by justus von liebig (1803–1873) on metal fulminates and some further developments in metal fulminates and related areas of chemistry. Eur J Inorg Chem. 2003;2003:4275–88.
6. Zhao L, Mak TCW. Silver(I) 1,3-butadiynediide and two related silver(I) double salts containing the C 4 2- dianion. J Am Chem Soc. 2004;126:6852–3.
7. Cataldo F, Casari CS. Synthesis, structure and thermal properties of copper and silver polyynides and acetylides. J Inorg Organomet Polym Mater. 2007;17:641–51.
8. Colmenero F. Silver oxalate: mechanical properties and extreme negative mechanical phenomena. Adv Theory Simulations. 2019;2:1–9.
9. Greenwood NN, Earnshow A. Chemistry of the elements. 2nd ed. Elsevier; 1997.
10. Shang Y, Chen S-L, Yu Z-H, Huang R-K, He C-T, Ye Z-M, et al. Silver(I)-based molecular perovskite energetic compounds with exceptional thermal stability and energetic performance. Inorg Chem. 2022;61:4143–9.
11. Atakol A, Svoboda I, Dal H, Atakol O, Nazır H. New energetic Silver(I) complexes with Nnn type pyrazolylpyridine ligands and oxidizing anions. J Mol Struct. 2020;1210:128001.
12. Atakol O, Fuess H, Kurtaran R, Akay A, Arici C, Ergun Ü, et al. Three new dinuclear silver(I) complexes derived from pyrazolyl type ligands: crystal structure and thermal decomposition. J Therm Anal Calorim. 2007;90:517–23.
13. Wang T, Zhang Q, Deng H, Shang L, Chen D, Li Y, et al. Evolution of oxidizing inorganic metal salts: ultrafast laser initiation materials based on energetic cationic coordination polymers. ACS Appl Mater Interfaces. 2019;11:41523–30.
14. Hammerl A, Klapötke TM, Rocha R. Azide-tetrazole ring-chain isomerism in polyazido-1,3,5-triazines, triazido-s-heptazine, and diazidotetrazines. Eur J Inorg Chem. 2006. https://doi.org/10.1002/ejic.200600100.
15. Klapötke TM. Chemistry of High-Energy Materials. 2nd ed. Walter de Gruyter GmbH & Co KG; 2017.
16. Shakirova OG, Lavrenova LG, Kurat'eva NV, Naumov DY, Daletskii VA, Sheludyakova LA, et al. Spin crossover in iron(II) complexes with tris(pyrazol-1-yl)methane. Russ J Coord Chem. 2010;36:275–83.
17. Reger DL, Foley EA, Smith MD. Mononuclear metallacyclic silver(I) complexes of third generation bis(1-pyrazolyl)methane ligands. Inorg Chem. 2009;48:936–45.
18. Bonfant G, Melegari M, Balestri D, Mezzadri F, Marzaroli V, Bassanetti I, et al. Supramolecular assemblies in silver complexes: phase transitions and the role of the halogen bond. Inorg Chem. 2020;59:4140–9.
19. Durá G, Carrión MC, Jalón FA, Manzano BR, Rodríguez AM. Formation of Mono-, Di- and trinuclear species in the self-assembly of bis(pyrazolyl)(pyridin-3-yl)methane ligands and metals with different coordination geometries. Eur J Inorg Chem. 2015;2015:5874–85.
20. Kitchen JA, White NG, Boyd M, Moubaraki B, Murray KS, Boyd PDW, et al. Iron(II) Tris-[N 4 -substituted-3,5-di(2-pyridyl)-1,2,4-triazole] complexes: structural, magnetic, NMR, and density functional theory studies. Inorg Chem. 2009;48:6670–9.
21. Arı E, Şahin N, Üstün E, Dündar M, Karcı H, Özdemir İ, et al. Synthesis, antimicrobial activity and molecular docking study of benzyl functionalized benzimidazole silver(I) complexes. JBIC J Biol Inorg Chem. 2023;28:725–36.
22. Barnabas MJ, Parambadath S, Nagappan S, Chung I, Ha CS. Silver (I)-Schiff-base complex intercalated layered double hydroxide with antimicrobial activity. Adv nano Res. 2021;10:373–83.
23. Njogu EM, Omondi B, Nyamori VO. Silver(I)-pyridinyl Schiff base complexes: synthesis, characterisation and antimicrobial studies. J Mol Struct. 2017;1135:118–28.
24. Krause L, Herbst-Irmer R, Sheldrick GM, Stalke D. Comparison of silver and molybdenum microfocus X-ray sources for single-crystal structure determination. J Appl Crystallogr. 2015;48:3–10.
25. Sheldrick GM. SHELXT – Integrated space-group and crystal-structure determination. Acta Crystallogr Sect A Found Adv. 2015;71:3–8.
26. Sheldrick GM. Crystal structure refinement with SHELXL. Acta Crystallogr Sect C Struct Chem. 2015;71:3–8.
27. Spek AL. Structure validation in chemical crystallography. Acta Crystallogr Sect D Biol Crystallogr. 2009;65:148–55.
28. Farrugia LJ. WinGX and ORTEP for Windows : an update. J Appl Crystallogr. 2012;45:849–54.
29. Macrae CF, Sovago I, Cottrell SJ, Galek PTA, McCabe P, Pidcock E, et al. Mercury 4.0 : from visualization to analysis, design and prediction. J Appl Crystallogr. 2020;53:226–35.
30. Koga N. Ozawa ' s kinetic method for analyzing thermoanalytical curves. J Therm Anal Calorim. 2013;113:1527–41.
31. Kullyakool S, Danvirutai C. Determination of kinetic triplet of the synthesized Ni 3(PO4)2.8H2O by non-isothermal and isothermal kinetic methods. J Therm Anal Calorim. 2014;3:1497–507.
32. Brown M. Reaction kinetics from thermal analysis. In: Brown M, editor. Introd to Therm Anal. 2nd ed. Dordrecht: Kluwer Academic Publishers; 2004. p. 181–214.
33. Breuer G. Handbuch der Präparativen Anorganischen Chemie. Stuttgart: Ferdinand Enke Verlag; 1954.
34. Patel JB, Cockerill FR, Bradford PA. Performance standards for antimicrobial susceptibility testing: twenty-fifth informational supplement. Clinical and Laboratory Standards Institute; 2015.
35. Onbas T, Osmanagaoglu O, Kiran F. Potential properties of Lactobacillus plantarum F-10 as a bio-control strategy for wound infections. Probiot Antimicrob Proteins. 2019. https://doi.org/10.1007/s12602-018-9486-8.
36. Linstrom PJ, Mallard WG. NIST Standard Reference Database Number 69. Natl. Inst. Stand. Technol. Gaithersburg MD,USA; 2011. Accessed 05 May 2025.
37. Gatehouse BM, Livingstone SE, Nyholm RS. Infrared spectra of some nitrato-co-ordination complexes. J Chem Soc. 1957;4222.
38. Celik S, Yurdakul S, Erdem B. Synthesis, spectroscopic characterization (FT-IR, PL), DFT calculations and antibacterial activity

of silver(I) nitrate complex with nicotinaldehyde. Inorg Chem Commun. 2021;131: 108760.
39. Scherrer P. Bestimmung der Größe und der inneren Struktur von Kolloidteilchen mittels Röntgenstrahlen. Nachrichten von der Gesellschaft der Wissenschaften zu Göttingen. 1918;26:98–100.
40. Reger DL, Foley EA, Smith MD. Synthesis of a tritopic, third-generation bis(1-pyrazolyl)methane ligand and its silver(I) complex: unexpected structure with high coordination numbers. Inorg Chem Commun. 2010;13:568–72.
41. Reger DL, Semeniuc RF, Smith MD. Metal complexes of 2,6-Bis[(pyrazol-1-yl)methyl]pyridine: the search for Aryl−Pyrazolyl embrace interactions as a synthon for crystal engineering. Cryst Growth Des. 2005;5:1181–90.
42. Qin J, Lei N, Ding H, Liu Y-P, Xu Y-P, Qian S-S. Syntheses, crystal structures, and fluorescence properties of Cd(II), Ag(I) complexes based on 3,5-bis(pyridin-2-yl)-4-amino-1,2,4-triazole. Synth React Inorg Met-Org Nano-Met Chem. 2016;46:968–74.
43. Parmar P, Mukherjee S, Kumar Singh V, Meikap BC. Thermokinetic analysis of sugarcane bagasse as a sustainable energy resource evaluation. Therm Sci Eng Prog. 2024;54:102836.
44. Prabhakaran SS, Swaminathan G, Joshi VV. Combustion and pyrolysis kinetics of Australian lignite coal and validation by artificial neural networks. Energy. 2022;242:122949.
45. Li Z, Jiang X, Zhu L, Chen F, Liu H, Ming L. New insights into the thermal degradation behavior of Hydroxypropyl-beta-cyclodextrin inclusion complexes containing carvacrol essential oil via thermogravimetric analysis. J Therm Anal Calorim. 2022;147:11301–12.
46. Spek AL. Single-crystal structure validation with the program PLATON. J Appl Crystallogr. 2003;36:7–13.
47. Saha S, Rajput L, Joseph S, Mishra MK, Ganguly S, Desiraju GR. IR spectroscopy as a probe for C-H···X hydrogen bonded supramolecular synthons. CrystEngComm. 2015;17:1273–90.
48. Steiner T. The hydrogen bond in the solid state. Angew Chemie Int Ed. 2002;41:48–76.

Publisher's Note Springer Nature remains neutral with regard to jurisdictional claims in published maps and institutional affiliations.